Fast Energy Storage Systems Comparison in Terms of Energy Efficiency for a Specific Application

JORGE TORRES [1], **PABLO MORENO-TORRES**[2], **GUSTAVO NAVARRO**[1], **MARCOS BLANCO**[1], **AND MARCOS LAFOZ**[1]

[1]CIEMAT, Spanish National Research Centre on Energy, Environment and Technology, 28040 Madrid, Spain
[2]Wynnertech S.L., 28906 Madrid, Spain

Corresponding author: Jorge Torres (jorgejesus.torres@ciemat.es)

ABSTRACT One of the key parameters to properly and accurately assess an energy storage system is the energy efficiency, which has a direct impact on the system performance and an indirect impact in its cost. In this paper, a methodology for comparing double-layer capacitors (EDLC) and kinetic energy storage systems (KESS) in terms of energy efficiency is proposed. This methodology, based on accurate loss models, takes real operating cycles into account, so a realistic result is obtained for each particular case. An accurate study of the losses of both technologies is accomplished during the paper, getting a complete model for EDLCs and KESSs, and obtaining efficiency maps for the whole range of operation points. Some conclusions about the convenience to use one or the other alternative and the best way to operate them are presented. In addition, a specific study case related to a wave energy power generation plant has been carried out in this paper, defining a methodology to select the energy storage requirements, calculating the round-trip efficiency and getting some recommendations related to the most appropriate operation strategy to take the most advantage of the energy storage system.

INDEX TERMS Fast energy storage system, supercapacitor, flywheel, energy efficiency.

I. INTRODUCTION

Electrical Energy Storage Systems (EESSs, or simply ESSs) are becoming of critical importance in many industrial sectors, with new applications and new commercial products being released every year. There are already many electrical energy storage technologies of different nature: chemical (fuel cells), electrochemical (batteries), electrostatic (supercapacitors), electromechanical (flywheels, compressed air and hydro pumped energy storage) and electromagnetic (superconducting magnetic energy storage) [1], [2]. Some of these technologies have already reached maturity and are commercially available, while others are still under development [3]. Another useful classification of EESSs is done based on the typical duration of their charge/discharge cycle: very short (less than a few seconds), short (seconds to minutes), medium (minutes to hours) and long (days) [1], [2]. This classification, shown in Table 1, is strongly related to the EESS energy and power density, and thus to its functionality within a given system. For instance, in power quality applications, peak shaving requires a medium time range ESS, while grid frequency control demands a faster technology.

Choosing the most appropriate energy storage technology for a given application is not a straightforward task, especially when the system characteristics imply that the operating cycle is both complex and variable. The decision becomes even more difficult when considering hybrid energy storage systems that combine at least two different technologies. Many economical and technical factors influence this choice, and an optimized design (based on criteria such as total cost, considering installation, operation and replacement costs) is not always achieved, sometimes because of lack of information regarding the different technologies.

This paper focuses on the named fast ESSs, i.e., those whose typical charge/discharge cycle is short. Namely, Electric Double Layer Capacitors (EDLCs) and Kinetic Energy Storage Systems (KESSs) based on flywheels. These two alternatives are comparable regarding Technology Readiness Level (TRL) [4] and provide similar performance in terms of energy, power and number of cycles. In other words, they can

TABLE 1. Electrical energy storage classification according to cycle duration (based on [1], [3]).

Cycle Duration	Quantity	Electrical Energy Storage
Very short	<10s	Capacitors, inductors
Short	1s to 15 minutes	EDLCs, KESS, SMES
Medium	5 minutes to 24 hours	Batteries: Li-ion, LA, NiMH, flow, etc.
Long	Days	Batteries, CAES, HPES

be considered competitors; although at present EDLCs have a larger market and are more popular than KESSs.

A comprehensive comparison of both alternatives is not the goal of this paper. Instead, this work focuses on describing a detailed methodology to assess both EESSs in terms of energy efficiency exclusively. This proposed methodology may be applied to different decision scenarios on its own, but also as part of a comprehensive comparison. The results corresponding to the case example included in this work can also illustrate how both EDLCs and KESSs perform in terms of energy efficiency – just "efficiency" for the rest of this paper – for those readers interested in a general conclusion. Besides, this paper deals only with Electric Double Layer Capacitors (EDLCs), thus leaving other types of supercapacitors, such as pseudo-capacitors and high voltage ceramic capacitors, out of its scope.

Energy efficiency is usually considered a secondary attribute in ESSs. Primary attributes are capacity (how much energy can be stored), specific energy/energy density (how much energy can be stored per unit of mass/volume), charging/discharging power (how much energy can be stored/drawn per unit of time) and useful life (how many charge/discharge cycles can be achieved before the systems degrades significantly), among others. However, efficiency can play a non-negligible role in some applications. For instance, higher efficiency in lithium-ion batteries means more runtime in your smartphone and more range in your electric vehicle. For fast ESSs, higher efficiency usually means that a smaller capacity is enough to achieve the desired goal, since less energy is wasted in the conversion process. In both cases, the higher the efficiency, the higher the available energy. In other words, the efficiency attribute could be considered as part of the usable capacity attribute, since the former improves the latter.

When talking about energy efficiency in complex non-linear systems, such as most ESSs, a single number does not suffice. Saying that an EDLC-based ESS has an average efficiency of 95% is not enough to stablish a fair comparison with other technologies, especially in applications with complex non-repetitive working cycles. There are many causes for this fact:

1. Efficiency depends on the operating point, namely on the State of Charge (SoC) of the system and on the instantaneous power drawn/injected on it. For EDLCs, this means that the efficiency is a function of voltage and current, while in the case of a KESS it depends on the speed and on the torque of the flywheel.

2. For each ESS, global efficiency is given by the product of the individual efficiencies of the different subsystems that integrate the entire system. For instance, the efficiency of an EDLC-based ESS depends on the EDLCs power losses and also on the interface converter power losses. Providing only the individual efficiency of the EDLCs is not fair, particularly for comparison purposes.

3. Efficiency also depends on the working cycle. Therefore, any efficiency value should be given referred to a specific working cycle. This is especially significant in the case of EDLCs, since their Equivalent Series Resistance (ESR), which models power losses within them, is frequency dependent.

Statement number 1 implies that single numbers should be avoided; 2D or 3D maps may be used instead to better describe the efficiency of a given ESS. Statement number 2 leads to the utilization of global efficiencies instead of individual efficiencies. Point number 3 suggests that efficiency values must be linked to a specified working cycle, a concept that we have named "smart efficiency". This work describes how to compare fast ESSs by obtaining smart global efficiency maps.

Most of the research works done in this area are focused in the calculation of efficiency at rated load which leads many times to unfair comparisons or insufficient in several applications in which the system does work at partial load and the efficiency is lower, see [5]–[10]. The main motivation of the paper is to define a methodology to get a complete efficiency map (similar to the ones shown in [11]–[15]) for energy storage technologies, in order to evaluate their performance in all the operation points of a specific application. That will allow a fair comparison of the different technologies.

The rest of the paper is organized as follows: In Section II, the hypotheses, assumptions and comparison scope of two ESS systems are presented. The loss model of an EDLC-based ESS and KESS-based ESS are proposed in Sections III and IV, respectively. In Section V, a comparison of both systems efficiency map and a previous conclusions are presented. Finally, a model for both systems and a study case in a real application is described in Section VI. Conclusions are given in Section VII.

II. COMPARISON SCOPE, HYPOTHESES AND ASSUMPTIONS

This section relates what factors were considered in this work, what factors were neglected or left out for simplicity, and what assumptions were made in the comparison process.

A. ESS GENERAL REQUIREMENTS

In this work, it has been considered that both ESSs must comply with the following prerequisites:
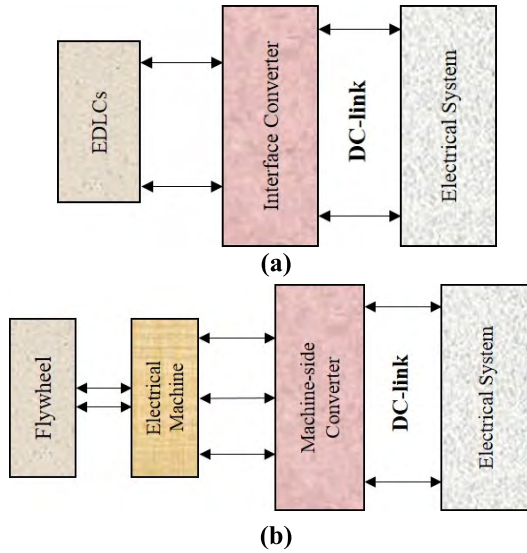
FIGURE 1. Basic layout of the two energy storage systems considered, both connecting to a generic electrical system through a 950V DC-link: (a) Supercapacitor-based ESS (EDLCs-ESS); (b) Kinetic Energy Storage System (KESS).

- The connection point for each ESS is a DC-link with rated voltage 950V, as shown in Fig. 1. In most applications, this DC-link would be connected to a 400V 50/60Hz grid through a grid-tie inverter.
- Both ESSs must have the same power and energy. This means that the design process must start with the EDLCs, since both magnitudes are coupled; i.e., it is not possible to increase one of them without increasing the other proportionally. Batteries suffer from the same limitation. In this sense, one of the advantages of KESSs is that the power and the stored energy are independent: the former is given mainly by the electrical machine power, while the latter is defined by the flywheel mass and speed.
- Energy and power requirements are defined as follows: 0.5kWh of usable energy and, at least 125kW of power when the system is fully charged (maximum). As maximum power depends on SoC in both technologies, the above specification means that maximum power at each operating point will be as illustrated in Fig. 2.

In EDLCs, minimum operating voltage is usually defined as half the rated voltage, which yields a little more than 75% of usable energy [2]. For the particular cell used in this work, described in section III:

$$E_{EDLC}[J] = \frac{1}{2} \cdot \left(C_0 + \frac{4}{3} \cdot k \cdot u \right) \cdot u^2 \quad (1)$$

$$SoC_{EDLC}[\%] = \frac{\left(C_0 + \frac{4}{3} \cdot k \cdot u \right) \cdot u^2}{\left(C_0 + \frac{4}{3} \cdot k \cdot u_{max} \right) \cdot u_{max}^2} \cdot 100\% \quad (2)$$

$$\left.\begin{array}{l} u_{min} = 0.6u_{max} \\ u_{max} = 2.65V \\ C_0 = 1850F \\ k = 350^F/_V \end{array}\right\} \Rightarrow \left\{\begin{array}{l} SoC_{EDLC,min} = 30.2\% \\ Usable\ energy = 69.8\% \end{array}\right. \quad (3)$$
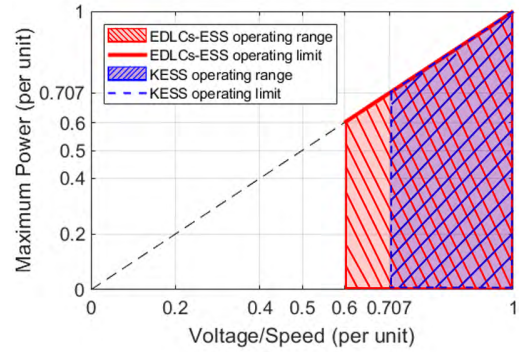

FIGURE 2. Maximum power as a function of voltage (EDLCs)/ speed (KESS).

where

E_{EDLC}	: Stored energy in EDLCs for a voltage level
C_0	: initial capacitance
k	: coefficient which represents the effects of the diffused layer of the EDLC
u	: EDLC operating voltage level
u_{min}	: EDLC Minimum operating voltage
u_{max}	: EDLC Maximum operating voltage
SoC_{EDLC}	: State of Charge of EDLC for a specific voltage
$SoC_{EDLC,min}$	: minimum EDLC SoC for a specific voltage
Usable energy	: EDLC usable energy

Similarly, common practice for KESSs consists in working with a minimum speed close to 70.7% of the rated speed, which provides exactly 50% of usable energy [16]. These two criteria are also adopted in this work:

$$E_{KESS}[J] = \frac{1}{2} \cdot J \cdot \omega^2 \quad (4)$$

$$SoC_{KESS}[\%] = \frac{\omega^2}{\omega_{max}^2} \cdot 100\% \quad (5)$$

$$\omega_{min} = \frac{\omega_{max}}{\sqrt{2}} \Rightarrow SoC_{KESS,min} = 50\% \quad (6)$$

where

E_{KESS}	: stored energy in KESS for a specific speed
J	: total inertia of the system
ω	: Flywheel Speed
ω_{min}	: minimum operating speed
ω_{max}	: maximum operating speed
SoC_{KESS}	: State of Charge of KESS for a specific speed
$SoC_{KESS,min}$	: minimum KESS SoC for a specific speed

B. EDLCs DEFINITION

In the case of the EDLCs, the above prerequisites must be complied in addition to the following:

- The basic unit used to build the EDLCs is a 3000F 2.7V cell, which is one of the most common supercapacitors and can be found from various manufactures [17]–[19].
- To provide an optimized voltage ratio in the EDLCs' interface converter, the maximum and the minimum operating voltage of the supercapacitors were chosen around [317 .. 633]V. This voltage range implies voltage ratios of [1/3 . . . 2/3] in the DC/DC converter, corresponding to convenient values of efficiency at the converter [20]. Therefore, the number of cells connected in series rises up to 240, yielding a voltage range of [382 .. 636]V when maximum operating voltage is limited to an average of 2.65V per cell, which is the criteria assumed in this paper. Notice that limiting the SCs maximum voltage implies increasing their useful life while minimizing balancing issues, at the cost of reduced useful energy.
- The usable energy provided by on single branch of 240 cells in series is 0.50kWh. Consequently, one branch is enough to fulfill the energy storage requirement.
- The maximum power delivered by one single branch of 240 cells in series reaches 125kW, considering a rated current value of 200A. Thus, no extra branches are needed to provide the required power.
- The frequency dependency of the EDLCs capacity is considered negligible in this paper.

C. KESS DEFINITION

Once the ELDC is defined, a KESS is designed to achieve the same values of energy and power. Therefore, the usable energy of the flywheel must be close to 0.5kWh, while the electrical machine rated power must reach at least 125kW, to be comparable to the EDLC system:

- Considering a speed range of [4500 .. 6500]rpm, the total inertia needed for the flywheel results:

$$J\left[kg \cdot m^2\right] = \frac{2 \cdot E_{KESS}[J]}{\omega_{max}^2 - \omega_{min}^2} = 15.0 \qquad (7)$$

Fig. 3 a) shows a 3D model for such a flywheel. Since the total inertia of the system is given by the sum of the rotor and the flywheel, the electrical machine must be designed first in order to define the inertia of the rotor. Moreover, the diameter of the flywheel ($\phi 750 \ mm$) is represented. This parameter is key in the calculation of the total inertia of the system.
- Regarding the electrical machine, the following design is proposed to fulfill the requirements of this particular KESS [21]. All characteristics of the KESS electrical machine is listed in Table 2. Fig. 3 b) shows the SRM 2D section. Moreover, the three phases of the SRM are represented with the letters A-B-C.
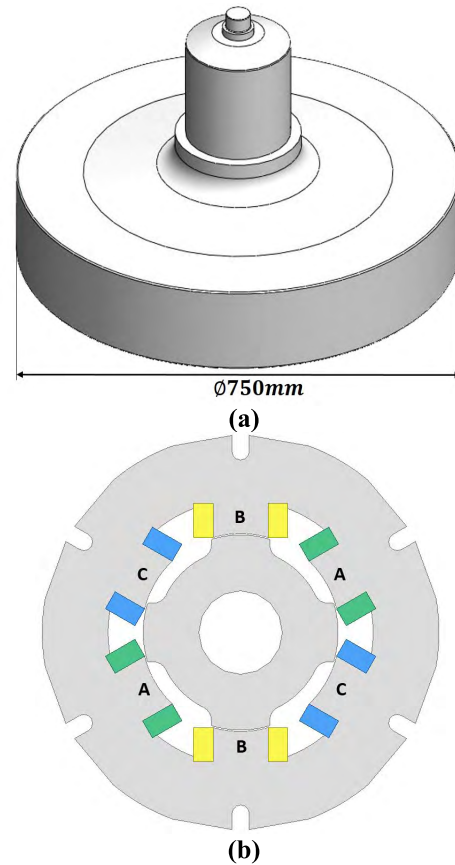

FIGURE 3. (a) 3D model of the flywheel; (b) 2D representation of the electrical machine.

TABLE 2. KESS electrical machine.

Type	Switched Reluctance Machine (SRM)
Rated power	125kW
Rated speed	6500 rpm
Topology	6/4
DC-link voltage	950V
Phase current	200A

III. LOSS MODEL OF A SUPERCAPACITOR-BASED ESS

An EDLC-based ESS comprises the supercapacitor cells and an interface DC/DC power converter. Power losses take place in both devices, as well as in the power cables connecting them, in the balancing system, and in the cooling system, and therefore they may be assessed individually for clarity.

A. SUPERCAPACITOR POWER LOSSES

In a single EDLC cell, ohmic losses take place in the positive and negative current collectors, in the positive and negative porous electrodes and in the separator [2]. All these power losses are usually represented by an Equivalent Series Resistance (ESR) when modeling an EDLC cell, as illustrated in Fig. 4. This ESR is not constant, and depends on the frequency of the current, on the cell voltage and on the
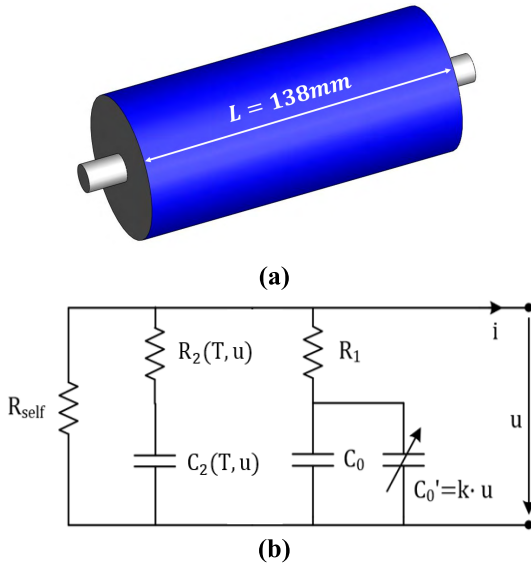
FIGURE 4. (a) 3D model of the supercapacitor; (b) Equivalent circuit of a supercapacitor cell used in this work [2], [22], [24].

cell temperature in a non-linear form [22]. In this paper last factor is neglected due to the installation of a cooling system which maintains the SCs in an operative temperature range [25°C–40°C], thus minimizing ESR variations.

Another source of losses in an EDLC cell is the self-discharge, which is a leakage effect dominated by redox reactions at the electrode surface through which electrons cross the double layer [23]. Self-discharge depends highly on voltage, temperature and aging, so it is more easily modeled by means of a voltage-controlled temperature-dependent current source, as shown in Fig. 4.

In most applications, supercapacitors cells are connected in series and parallel arrangements (modules) to provide the required voltage and energy/power. This means that extra ohmic losses take place in the contact resistance of those connections. However, this resistance is approximately constant, since it only varies with the temperature.

As mentioned above, a supercapacitor is not a linear device; its properties depend on both the voltage and the frequency. In this paper a frequency-dependent resistance (ESR) is analyzed to calculate the supercapacitor power losses. There are two different frequency ranges in the spectrum of the supercapacitor current: A low frequency current related to the supercapacitor's operational mode and charge-discharge cycle and a high frequency current due to the power converter ripple. In general form, the instantaneous power of the resistor ESR $P_{ESR}(t)$ carrying a current i_{SC} is:

$$P_{ESR}(t) = u_{ESR_{SC}}(t) \cdot i_{SC}(t) \qquad (8)$$

where

P_{ESR} : instantaneous power losses of the resistor ESR

$u_{ESR_{SC}}(t)$: voltage of the resistor ESR

$i_{SC}(t)$: instantaneous current on SCs system

Considering the current i_{SC} as a periodic function with a period T, this current can be expressed as a Fourier series:

$$i_{SC}(t) = \sum_{k=0}^{+\alpha} I_{SC}(k) \cdot sin(kwt + \varphi_k) \qquad (9)$$

where

$I_{SC}(k)$: Current value for each harmonic

w : Angular frequency [rad/s]

The voltage across ESR can be also expressed as a Fourier series:

$$u_{ESR_{SC}}(t) = \sum_{k=0}^{+\alpha} ESR(kw) \cdot I_{SC(k)} \cdot sin(kwt + \theta_k) \qquad (10)$$

where

$u_{ESR_{SC}}$: voltage across the ESR

$ESR(kw)$: ESR value for each frequency

So, from equations (8), (9) and (10), the instantaneous power dissipated on the resistor ESR is:

$$P_{ESR}(t) = \sum_{k=0}^{+\alpha} I_{SC(k)} \cdot sin(kwt + \varphi_k)$$
$$\cdot \sum_{k=0}^{+\alpha} ESR(kw) \cdot I_{SC(k)} \cdot sin(kwt + \theta_k) \qquad (11)$$

Using the Lagrange identity and the orthogonal property of the sin and cos functions [2], the total average power depends on the frequency spectrum of the capacitor current and, consequently of the equivalent resistance dependent of that frequency. The expression of these total power losses is:

$$P_{ESR}(t) = I_{rms}^2 \cdot \left[\sum_{k=0}^{+\alpha} ESR(kw) \cdot \frac{I_{SC(k)}^2}{I_{rms}^2} \right] = I_{rms}^2 \cdot ESR(eq) \qquad (12)$$

where

I_{rms} : r.m.s. value of the current

$ESR(eq)$: Equivalent ESR

The first step for calculating these frequency related power losses is to develop a frequency model of a supercapacitor. A model implemented in Matlab-Simulink environment [25] provides a frequency characterization of the capacity and the ESR of a supercapacitor cell, as shown in Fig. 5. These measurements have an error of 7% with respect to the manufacturer's values.

Once the coefficients and the frequency spectrum are determined, the power losses evolution over time is calculated using (12). The ESR losses have been calculated for a particular operation cycle, periodic with frequency 0.7 Hz, described in Section V. Therefore, the ESR losses for that cycle and the partial efficiency of the system could be calculated using (12) and [24], and shown in Fig. 6 a) and b), respectively.
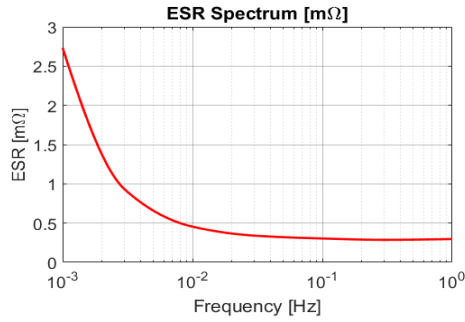
$$\eta_{P_{ESR}} = \frac{I \cdot U}{I \cdot U + P_{ESR}} \qquad (13)$$

FIGURE 5. ESR evolution as a function of the frequency.
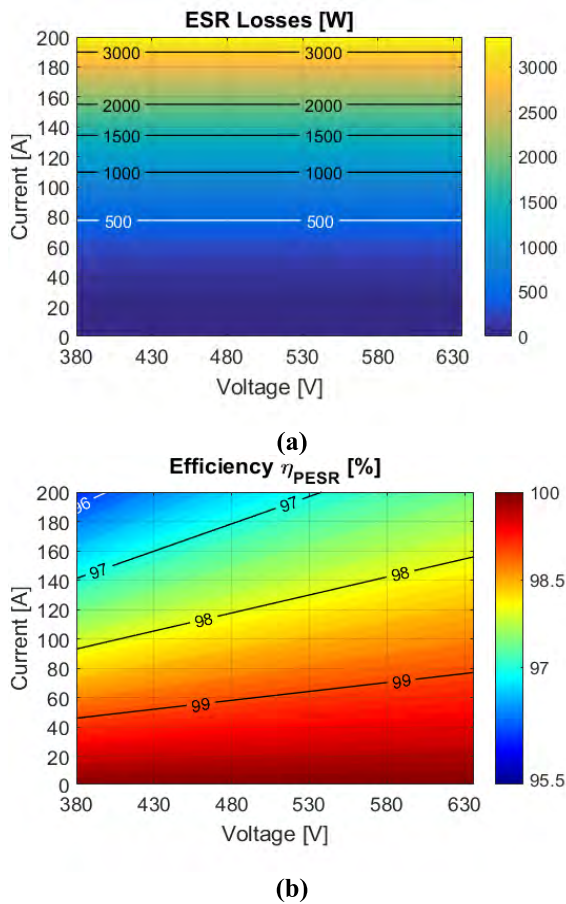

(a)

(b)

FIGURE 6. (a) ESR losses evolution as a function of voltage and current operation; (b) ESR theoretical losses compared to the EDLCs power.

where

$\eta_{P_{ESR}}$: r.m.s. current on the SCs system
U : voltage of the SCs system
I : r.m.s. current on the SCs system

B. INTERFACE BALANCING LOSSES

In this paper, a balancing system has been used [17], [26]–[28]. This device makes the balancing process from $V_{min} \sim 2.57$ V per cell, which implies no balancing losses below this voltage (zero power consumption). This type of balancing is an ELDC maximum voltage protection,

so their use could be negligible in some operation cycle and has to be taken into account in specific situations as UPS application. The balancing current and dissipation resistance are known, so the cell balancing losses can be calculated using the Joule formula (14). The results are shown in Fig. 7.

$$P_{balancing} = R_{eq.} \cdot I_{eq.}^2 \qquad (14)$$

where

$P_{balancing}$: balancing losses
$R_{eq.}$: balancing resistance
$I_{eq.}$: balancing current

As the above figure displays, the equalization losses could be neglected compared with the other losses of the EDLCs system.
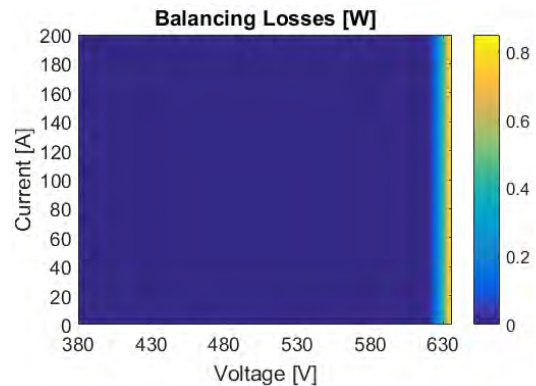

FIGURE 7. Balancing losses evolution as a function of the voltage and current operation.

C. COOLING LOSSES

Analyzing the EDLCs inner losses, the system requires a cooling device which decreases the temperature of the supercapacitors in order to reduce their degradation and extend their life time [17]. A cooling turbine will operate from a certain power, since natural convection is enough below those power requirements. The cooling flow needed has been calculated using an electrical equivalent model implemented in Matlab-Simulink environment [25], [29]–[32]. The results from this model are checked with a fluid dynamics model made on a Computational Fluid Dynamics (CFD) program [33] and, with these results, a commercial turbine has been chosen. In addition, a turbine regulation curve has been set, depending on the power required by the application, in order to increase the efficiency of the system. The aforementioned conditions of turbine regulation are fixed to maintain a suitable temperature for the EDLCs system. The power consumption of the turbine is depicted in Fig. 8. Cooling losses are negligible compared with the electric losses due to the internal resistance (ESR).

D. CONNECTION INTERFACE LOSSES

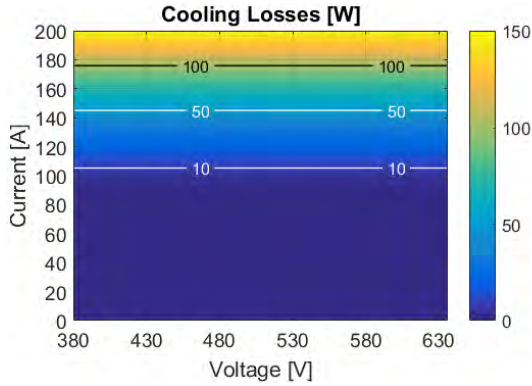In order to calculate the bus bars losses [34], the first step is to work out their resistance value. The geometrical

FIGURE 8. Cooling consumption as a function of the voltage and current operation. Dependent on the current level but not on the SoC.

configuration, the current and the section of the bars are needed to define the resistance of the buss bar, as shown in (15).

$$R_{busbar} = \frac{\rho \cdot l}{S} \qquad (15)$$

where

$R_{bus\ bar}$	: Resistance of the bus bar
ρ	: electrical resistivity of aluminum
l	: bus bar length
S	: buss bar cross-section

After that, the losses map for the supercapacitors system is determined using the Joule losses formula (16). The results are shown in Fig. 9, respectively.

$$P_{bus\ bars} = R_{bus\ bar} \cdot I^2 \cdot n_{SC} \qquad (16)$$

where

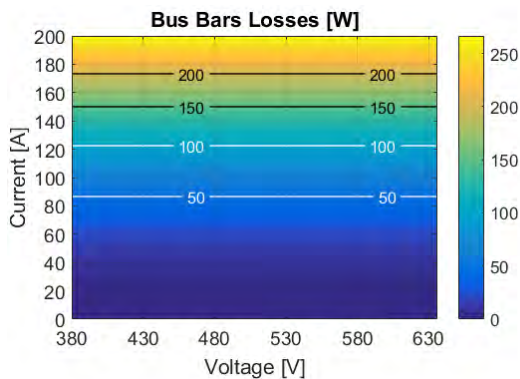|	
$P_{bus\ bars}$	: bus bars losses
n_{SC}	: number of EDLCs

FIGURE 9. Connection interface losses as a function of the voltage and current operation. Dependence just on the Joule effect losses.

E. INTERFACE POWER CONVERTER LOSSES

As energy efficiency is dependent also on the power electronics topology, the analysis must consider it. A bidirectional DC/DC power converter interconnects two different

DC systems, SCs and DC-link as shown in Fig. 10. This power converter basically consists of an input filter, power electronic modules and an output filter. In this case a boost-buck topology is selected since no isolation is required [20] and the bidirectional current.
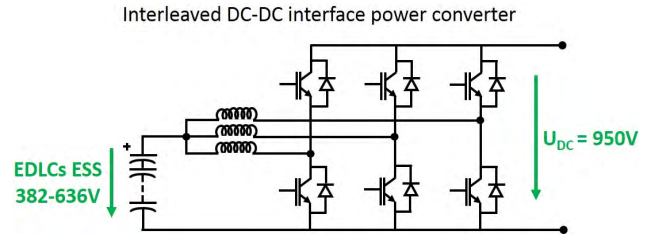

FIGURE 10. Supercapacitor-based energy storage system with an interleaved DC/DC interface power converter.

The DC/DC power converter is preferred to operate in DCM (discontinuous conduction mode) to minimize power losses, a multiphase current-controlled buck-boost converter [35] connects the EDLCs by means of three parallel inductances.

The modulation technique used is PWM with interleaving [36]. The interleaving technique connects DC/DC converters in parallel (or different branches of the same converter) to share the power flow between two or more conversion chains (three conversion chains in this case). Its main advantages are constant switching frequency, current ripple reduction and capacitor and inductor size/weight shrinkage [37]. Besides, the interleaved topology helps improving energy efficiency.

A Matlab-Simulink model has been implemented with two main objectives: first, to design a proper interface converter (including design tasks such as the calculation of the inductance values or the selection of the proper commercial IGBT branch or the proper cooling turbine); and second, to calculate the power converter losses (including switching losses and conduction losses in the IGBTs and diodes, which are calculated as it is described in [38]). In particular, three IGBTs branches composed by three SEMIKRON SKM400GB17E IGBT power modules [39] have been considered. The power electronics losses (including the cooling turbine consumption) have been evaluated and shown in Fig. 11 a).

$$\eta_{P_{converter\ EDLCs}} = \frac{I \cdot U}{I \cdot U + P_{converter\ EDLCs}} \qquad (17)$$

where

$\eta_{P_{Converter\ EDLCs}}$	: Converter efficiency compared to the EDLCs
power $P_{Converter\ EDLCs}$	: EDLCs power converter losses

Fig. 11 a) shows the power converter losses as a function of the voltage and current through the EDLCs. Similarly, Fig. 11 b) shows the power converter efficiency as a function of this voltage and current, calculated using equation (17). Power converter losses are in the same order than electric losses due to internal resistance (ESR).
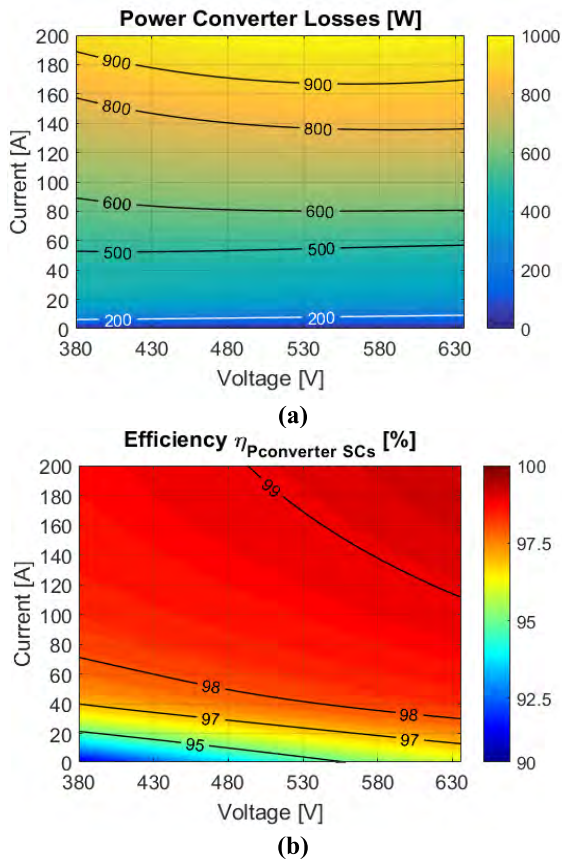
FIGURE 11. (a) Interface power converter losses as a function of the voltage and current operation; (b) Converter efficiency compared to the EDLCs power. Losses very dependent on the current, not on the SoC.

IV. LOSS MODEL OF A FLYWHEEL-BASED ESS

KESS system studied in this paper comprises a high strength steel alloy flywheel, a Switched Reluctance Motor/Generator (SRM), a hybrid angular contact ball bearings, a permanent magnet rim (magnetic levitation), a chamber case to cover the flywheel and a vacuum pump to maintain the operation pressure.

The main losses to be considered in this type of storage device are: friction losses on bearings, windage losses around the spinning elements (rotor and flywheel) [40], copper losses on coils, iron losses on SRM (stator and rotor) [41], [42], vacuum leakage losses, cogging losses due to the magnetic levitation and the losses on power electronics. They are accurately described next.

A. BEARING LOSSES

The process to calculate the bearing losses is based on the method used by the manufacturer SKF in their bearings [43]. The input data are: type of bearing (defined by the application, load rating and operation speed of the device) and the equivalent dynamic bearing load. The friction torque expression is given by:

$$T_{bearing}(\omega) = \frac{1}{2}\mu P_{eq}(\omega) \qquad (18)$$

where

$T_{bearing}$: friction torque as a function of angular speed

μ : friction coefficient, obtained from SKF data and depending on the type of bearing, its lubrication and the material type of the rolling elements inside

$P_{eq}(\omega)$: equivalent dynamic bearing load as function of the speed

ω : angular speed of the flywheel

The equivalent dynamic bearing load is obtained from the radial and axial forces exerted on the bearings. The axial load is a percentage of the residual weight of the flywheel (usually 20% of its weight), since it has been designed with a rim of magnets that supports most of the flywheel's weight. Therefore, the axial force exerted on the bearings is:

$$F_{axial} = 0.20 \cdot Mg \cong 1000 \ N \qquad (19)$$

where

F_{axial} : axial force exerted on the bearings

M : flywheel and rotor weights

g : standard gravity

Regarding the radial force, the process is based on the dynamic balance calculation of the system. Centrifugal force due to the imbalance of the flywheel is equaled to the force that supports the bearing.

$$F_r = N \cdot K_{bearing} \cdot x^{3/2} \qquad (20)$$

$$K_{bearing} = 6 \cdot 10^{-6} \sqrt[3]{\frac{F_r^2}{100Z^2 d_b(sin\alpha)^5}} \qquad (21)$$

where

$K_{bearing}$: nonlinear stiffness of bearings

N : number of bearings

x : dynamic unbalance of the system due to the speed

d_b : roller ball diameter

F_r : radial force exerted on bearings

Z : number of roller balls

α : angular contact angle of roller balls

The radial force on the bearings (20) and their stiffness (21) are extracted from [16]. Following, the imbalance of the flywheel (23) is calculated for the speed operation range and after that, using (20) the radial force on the bearings as well.

$$F_{cent} = M \cdot \omega^2 \cdot (x + u) \qquad (22)$$

$$x = \frac{u}{\frac{2 \cdot K_{bearing}}{M \cdot \omega^2} x^{1/2} - 1} \qquad (23)$$

where

F_{cent} : centrifugal force

u : static unbalance of the system due to manufacture process

Once the radial forces for the speed range of the device are determined, the calculation factors X and Y are worked out according to the SFK [43]. After that, the equivalent dynamic load values are defined according to:

$$P_{eq}(\omega) = X(\omega) \cdot F_r(\omega) + Y(\omega) \cdot F_{axial} \qquad (24)$$

where

$X(\omega)$ and $Y(\omega)$: SKF calculation factors

Finally, the bearing friction torque is determined and then the loss map (25), shown in Fig. 12.

$$P_{bearing} = T_{bearing} \cdot \omega \qquad (25)$$

where

$P_{bearing}$: bearing friction losses

Figure 12 presents the variation of bearing losses with the torque and the speed. The main variation is due to the speed, which corresponds to the SoC in flywheels. These losses are one order of magnitude lower than iron losses and power converter losses.
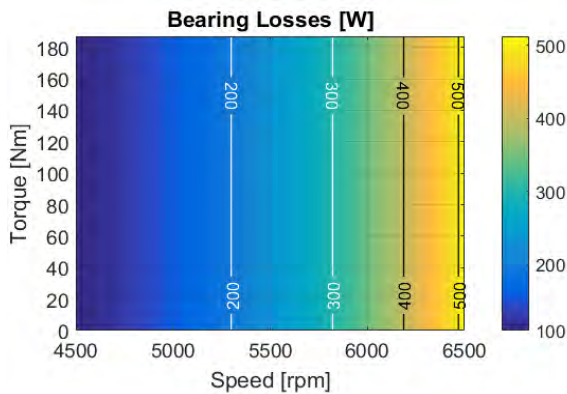

FIGURE 12. Bearing losses evolution as a function of speed and torque operation. Dependent on speed but not on the torque.

B. WINDAGE LOSSES

The first step in the aerodynamic losses calculation process is to determine the evolution of air density inside the system as a function of operating temperature and pressure. A correction of the ideal gases law is used, in which terms of relative humidity are included (correlation of Jones, 1978 [44]).

The next step consists in dividing the system geometry into several subsystems listed in Table 3 and shown in Fig. 13, reducing an aerodynamic problem with high complexity (a turbulent 3D model would have to be implemented) and long calculation time into several 2D and axial-symmetric (AS) models with small control volumes [45], [46], analyzed with a CFD tool (ANSYS-Fluent [33]) that allows to calculate the losses of the whole system using the principle of superposition [47].

Once the windage losses evolution respect to the operating pressure and speed is determined, the losses map and partial efficiency could be calculated. The results of losses, extracted from (26), are shown in Fig. 14. Aerodynamic losses at

TABLE 3. List of implemented CFD simulations, main parameters and type of turbulence models used.

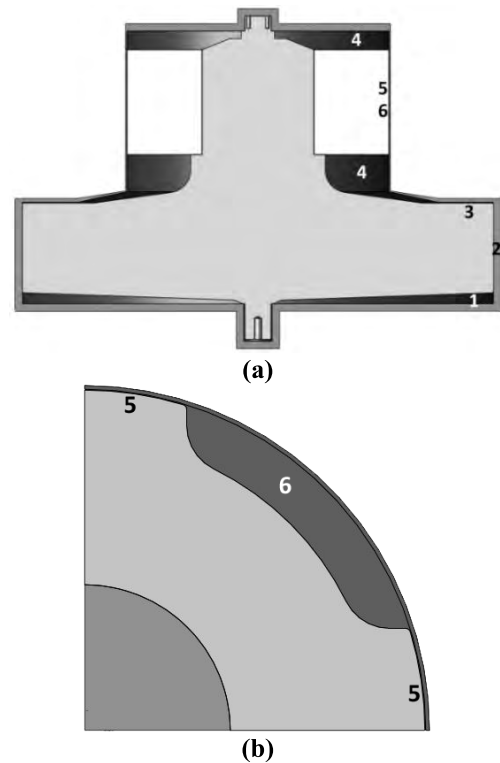| Number/Name	Model Type	Turbulent model	Problem Type
1. Two discs flow	AS	Transition SST	Batchelor flow [48]–[50]
2. Flywheel-case	2D	Laminar	Couette flow
3. Two discs flow	AS	Transition SST	Batchelor flow [48]–[50]
4. Two discs flow	AS	Transition SST	Batchelor flow [48]–[50]
5. SRM-chamber	2D	Laminar	Couette flow [45], [46]
6. SRM inner	2D	Transition SST	Recirculation flow [45], [46]

(a)

(b)

FIGURE 13. CFD simulation scheme: (a) Flywheel and SRM fluid dynamic problems listed in Table 3; (b) SRM control volume considered for simulation 5 and 6.

the working pressure of 1.25mbar (125 Pa) are considered negligible for the whole range of operation.

$$P_{windage} = T_{windage} \cdot \omega \qquad (26)$$

where

$T_{windage}$: Friction torque due to the aerodynamical losses

$P_{windage}$: Windage losses

C. VACUUM PUMP LOSSES

When calculating pump losses, the pressure operation range needs to be established. In this case, it is defined from 1 mbar (100 Pa) to 25 mbar (2500 Pa). After that, a vacuum pump which satisfies the technical characteristics (pump model: Rotary vane pump RZ 2.5 [51]) is selected and simulated
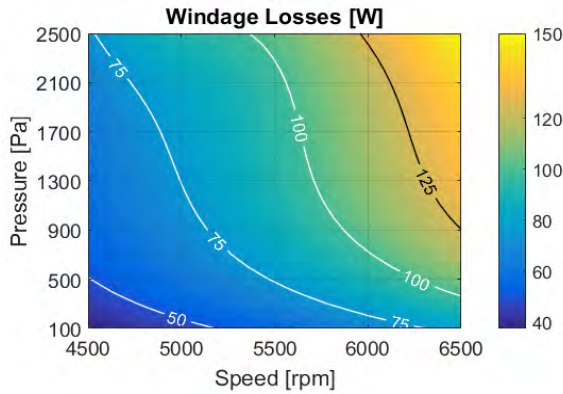
FIGURE 14. Windage losses evolution as a function of the speed and pressure. Only relevant when pressure is not reduced.

according to the air volume around the flywheel. The results determine the operation time of the pump to maintain the working pressure in the system. Finally, the power consumption is calculated and shown in Fig. 15.
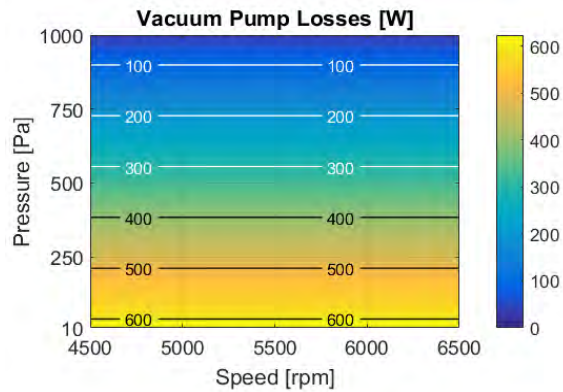

FIGURE 15. Vacuum pump losses evolution as a function of the speed and pressure. Only dependence of pressure level.

The operation pressure is chosen so that the sum of all the corresponding power losses (windage and vacuum pump losses) is minimized. The operating pressure is fixed in 5 mbar (500 Pa) where the vacuum pump power losses is 320W.

D. COPPER LOSSES

Although this methodology could be extended to any type of electric machine, in this paper a Switched Reluctance Machine (SRM) is analyzed. This type of machine is especially suitable for flywheel applications due to its robustness, low free-wheeling losses and absence of windings on magnets in the rotor, appropriate for high speeds.

An accurate study of the electric machine requires to consider power electronics together, as well as, in the particular case of SRMs, the phase activation and deactivation angles of each phase in order to maximize the efficiency and the mechanical torque [21], [52], [53].

A complete model has been developed and implemented in Matlab-Simulink environment [25] comprising: SRM, flywheel mass and power converter [41]. This model provides a current profile of each phase, depending on the power supplied and the speed of the device, in order to quantify the skin and proximity effects as well as the Joule effect losses on coils. Once the current profile is obtained, a postprocessing has been programmed, using a FFT function, in order to calculate the frequency spectrum.

Next step is to calculate the skin and proximity effect coefficients which determine their influence on the DC resistance value [52], [54]. In this design the coils have been manufactured with Litz wire which has a very low AC resistance and therefore, less copper losses than a conventional one.

The equations for the aforementioned coefficients are defined in (27), (28), (29) and (30). These factors are function of the switching current frequency. Therefore, in order to calculate the AC resistance value, the superposition principle is applied.

$$\varphi(x) = x \frac{\sinh(2x) + \sin(2x)}{\cosh(2x) - \cos(2x)} \qquad (27)$$

$$\psi(x) = 2x \frac{\sinh(x) - \sin(x)}{\cosh(x) + \cos(x)} \qquad (28)$$

$$x = \frac{H \cdot n}{1000} \left[\frac{w}{b} \pi f \sigma \mu_0 \mu_r \right]^{1/2} \qquad (29)$$

$$k_{i,AC} = \varphi_i + \frac{m^2 - 1}{3} \psi_i \qquad (30)$$

where

H	: height of the subconductors
x	: non-dimensional sin effect factor
n	: number of the parallel subconductors in radial direction
w	: width of subconductors
b	: width of the coil
f	: switching frequency
σ	: electrical conductivity of the copper wire
μ_0	: permeability of free space
μ_r	: relative permeability of copper
m	: number of conductor layers
$k_{i,AC}$	: AC coefficients of each frequency term
$\varphi(x)$ and $\psi(x)$	: skin and proximity effect coefficients

Once the coefficients and the frequency spectrum are determined, the losses evolution per electric revolution and phase are calculated (31) respect to the speed and power supplied, as shown in Fig. 16. Unless multiwire cable is used, the copper losses can reach high levels, one order of magnitude higher than the already presented in Figure 16.

$$P_{copper} = \left[\sum_{i=1}^{\infty} k_{i,AC} \cdot I_i^2 \right] R_{DC} n_{coils} \qquad (31)$$

where

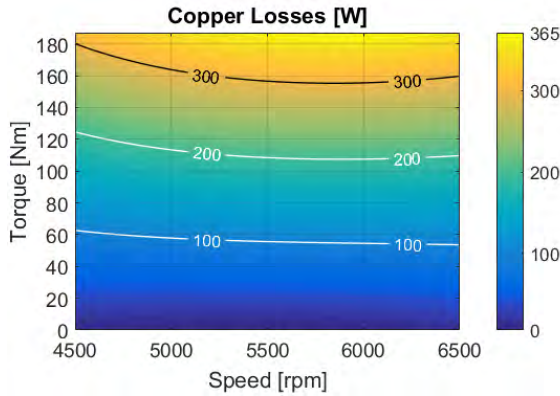|	
P_{copper}	: copper losses per electrical revolution
I_i	: frequency term of the AC current
R_{DC}	: DC resistance of the coils
n_{coils}	: number of coils by phase

FIGURE 16. Copper losses evolution as a function of the speed and torque operation. Torque (current) dependence.

E. IRON LOSSES

There are different methods to calculate the iron losses in a SRM [55]. Those based on analytical equations with or without electromagnetic simulations in FEM programs [56]–[59] and empirical methods, which employ measurements on the real machine [60], [61]. In this paper, analytical methods based on electromagnetic simulations are described and used. The aforementioned methods are basically: those based on the Bertotti equation and the most advanced ones, based on a 3D magnetic characterization of the rotor and stator material, also called Loss Surface models [58], [59]. This characterization is based on an evolution of the magnetic field density as a function of the magnetic field intensity and the derivative of magnetic field respect to time. The difference between them is mainly based on the switching frequency consideration. In Bertotti method, the switching frequency is constant, while the others use the derivative of the magnetic flux.

In this paper, a material (NO20-13 [62], [63]) which has a complete magnetic characterization [64], [65], has been used in order to employ an advanced calculation method based on Loss Surface models. The model has into account the switching frequency of the system which in SRM is not constant in the operation range.

Once the electromagnetic model is made and the current profile on each phase is calculated, the losses in the rotor and the stator of the machine are evaluated [66]. Knowing the value of the magnetic flux in each point, these losses are assessed.

The iron losses obtained are the most relevant component of the losses. They are a function of torque and speed of the device, but more dependent on torque (related to

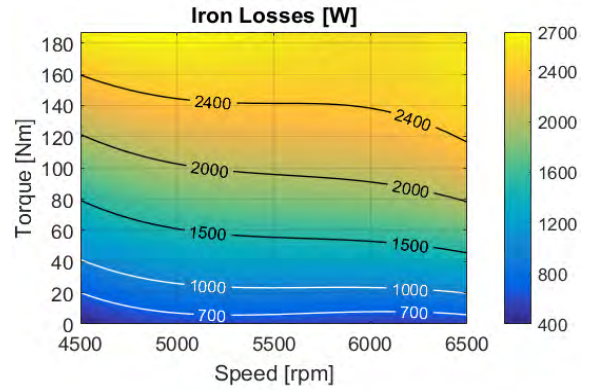the current) than on speed (related to the frequency), as it is shown in Fig. 17.

FIGURE 17. Iron losses evolution as a function of the speed and torque operation. More dependent on torque (current) than on speed (frequency).

F. PERMANENT MAGNET RIM LOSSES

The system incorporates a permanent magnet rim (magnetic levitation) which reduces the axial load on the bearings, leading to a reduction in bearing losses. The cogging losses are considered negligible with respect to the other losses since the magnetic flux density at the magnets airgap is in the range of 0.2T and no high frequencies are high presented.

G. MACHINE-SIDE POWER CONVERTER LOSSES

The topology on the machine-side converter is shown in Fig. 18. Three half-bridge IGBT are considered, one connected to each SRM electric phase [67]. Although other alternative topologies exists (such as Miller topology [53]), these topologies are focused on reduce the number of semiconductors at the expense of losing control flexibility and phase independence. It is preferred to keep full controllability by means of the half-bridge topology.
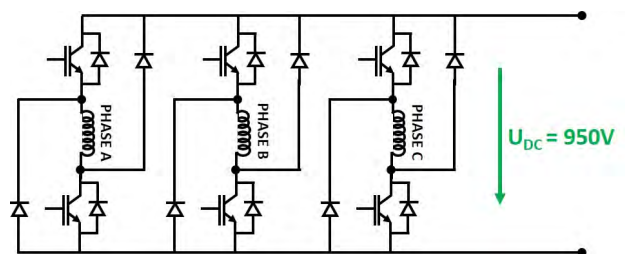

FIGURE 18. Flywheel-based energy storage system with a 3 H-bridge machine-side power converter.

The corresponding Matlab-Simulink model of the SRM and its (machine-side) power electronic converter has been implemented with the same objectives as the Matlab-Simulink model mentioned in sub-section III-E (to design the power converter and to calculate the power converter losses according to [38]). In particular, SEMIKRON

SKiiP 1203 GB172-2DFL IGBT power modules [68] have been considered.

The power electronics losses (including the cooling turbine consumption) have been evaluated as it is shown in Fig. 19 a), as a function of the speed (related to the commutation losses) and torque (related to the conduction losses) in the flywheel, being higher the dependence on torque than on speed. Similarly, Fig. 19 b) shows the power converter efficiency as a function of this speed and torque. This efficiency is calculated using the expression (32). From the figure it is obtained that power converter losses are at the same level than iron losses.
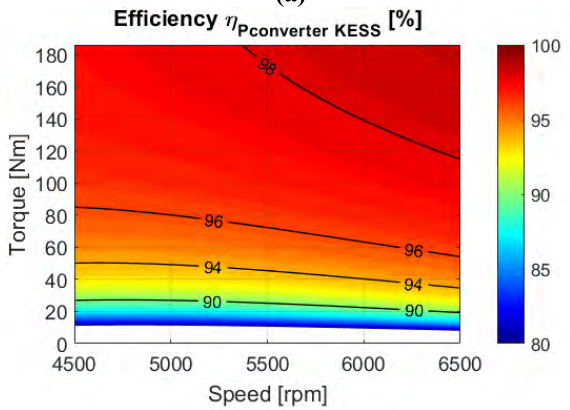
$$\eta_{P_{converter\ KESS}} = \frac{T \cdot \omega}{T \cdot \omega + P_{ConverterKESS}} \quad (32)$$

where

|	
$\eta_{P_{Converter\ KESS}}$	: converter efficiency compared to the KESS mechanical power
$P_{Converter\ KESS}$	: KESS power converter losses
T	: Mean torque of the flywheel
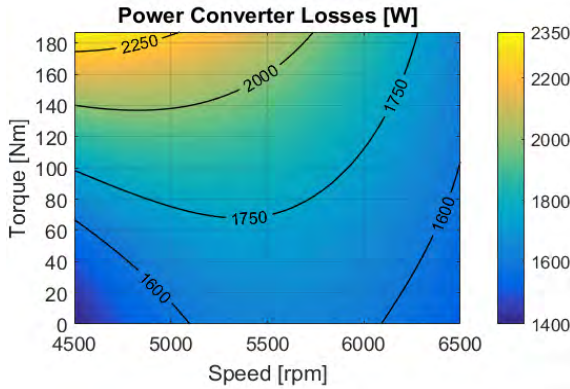
FIGURE 19. (a) Interface power converter losses as a function of the speed and torque operation; (b) Converter efficiency compared to the KESS mechanical power.

V. COMPARISON OF EDLC AND KESS LOSSES AND EFFICIENCY MAP

Once the losses of both devices have been determined, the total losses are calculated applying the superposition
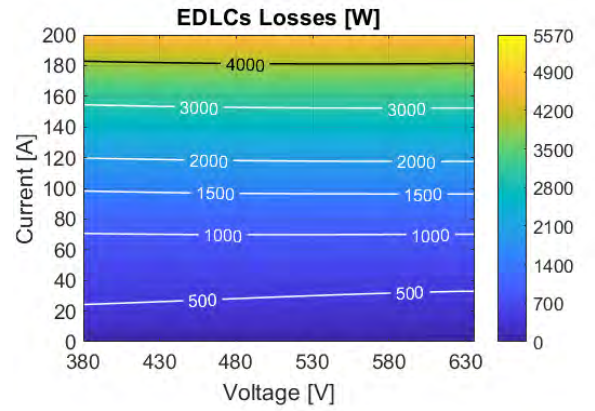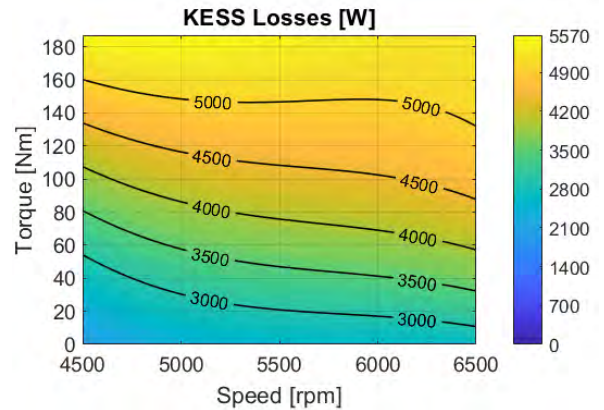
FIGURE 20. (a) EDLCs losses as a function of voltage and current; (b) KESS losses as a function of speed and torque.

principle, as shown in (33) and (34).

$$P_{EDLCs} = \sum P_i = P_{ESR} + P_{balancing} + P_{cooling}$$
$$+ P_{bus\ bars} + P_{converter\ EDLCs} \quad (33)$$
$$P_{KESS} = \sum P_i = P_{Converter\ KESS} + P_{iron} + P_{copper}$$
$$+ P_{vacuum\ pump} + P_{windage} + P_{bearing} \quad (34)$$

where

P_{EDLCs}	: EDLCs total losses as a function of the voltage and current operation
$P_{cooling}$	: cooling losses in EDLC system
P_{KESS}	: KESS total losses as a function of the speed and torque operation
P_{iron}	: iron losses in KESS system
$P_{vacuum\ pump}$	: vacuum pump consumption

As the previous sections display, there are several considerations related to the technologies that must to be taken into account in the efficiency calculation:

- The main losses in KESS system are the iron and converter losses.
- The main losses in EDLCs system are ESR and converter losses.

Fig. 20 a) illustrates the EDLCs losses as a function of voltage and current. Similarly, Fig. 20 b) displays KESS losses as a function of speed and torque.

As in the previous section, the efficiency of each system is calculated with the same equation. In the EDLCs system, equation (35) is used. In KESS case, the equation (36) has been utilized.

$$\eta_{EDLCs} = \frac{I \cdot U}{I \cdot U + P_{EDLCs}} \qquad (35)$$

$$\eta_{KESS} = \frac{T \cdot \omega}{T \cdot \omega + P_{KESS}} \qquad (36)$$

where

η_{EDLCs} : efficiency of the EDLCs system as a function of the current and voltage operation

η_{KESS} : efficiency of the KESS system as a function of the speed and torque operation

FIGURE 21. (a) EDLCs efficiency map related to the EDLCs output power; (b) KESS efficiency map related to the KESS mechanical power.

As the Fig. 21 a) and b) display, there are some considerations related to both technologies that should be considered in the process of selecting an ESS:

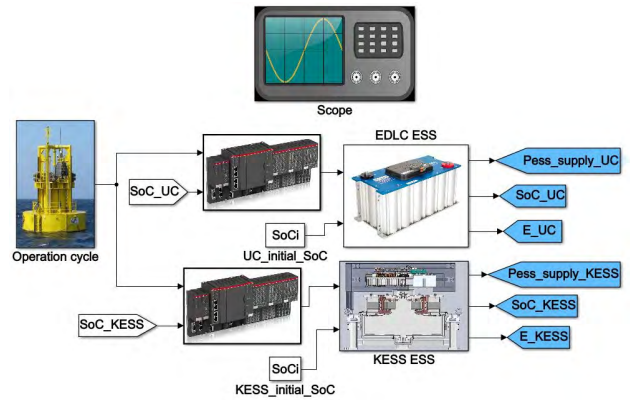- Generally speaking, power losses increase with power level both in EDLCs and KESS.

FIGURE 22. Matlab Simulink model of the cycle and ESSs.

- For high SoC, EDLC have the highest efficiency around 50% of power (current) while KESS have the highest efficiency at rated power (torque). Therefore, EDLCs have better performance at partial load than KESS. The efficiency of KESS at partial load could be improved with the introduction of a 'Stepped Switching' control strategy, as defined in Section VI.B.
- The EDLCs efficiency depends less on the power level (torque/current) than the KESS efficiency. For example, at 100% SoC (6500 rpm in KESS and 630V in EDLC), a power reduction from 100% to 50% makes the efficiency drop 4% in KESS, while EDLCs benefit from 1% increase.
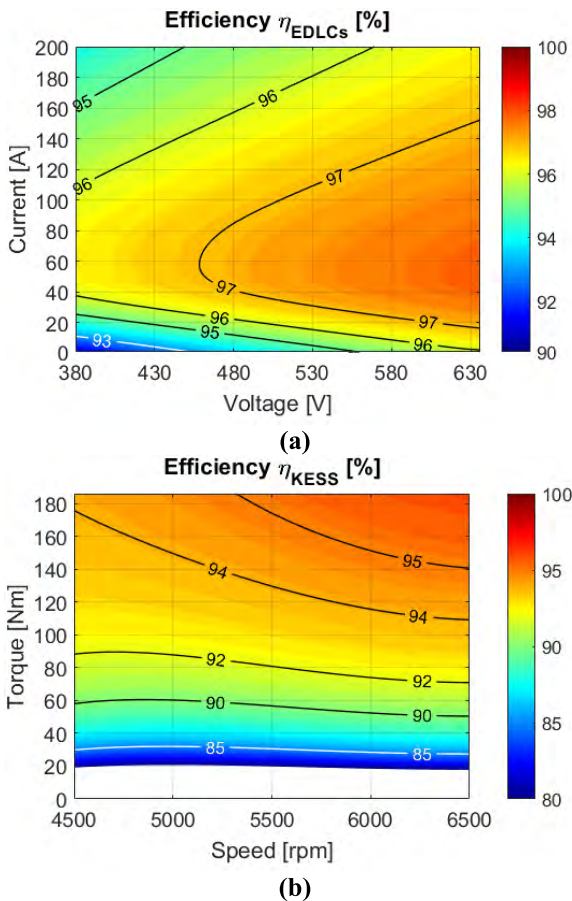
VI. ENERGY EFFICIENCY COMPARISON IN REAL OPERATING CYCLES

There are several real applications where this type of energy storage technologies are suitable, such as: grid stability, dynamic voltage control, fault management, traction regenerative braking, frequency stability, reduction of power oscillation in renewable generation [1], [2]. The application of compensating power oscillation in renewable power generation has been chosen as study case, in particular the generation scenario produced by a Wave Energy Converters (WECs) [69], [70].

A. DESCRIPTION OF A MODEL FOR THE ANALYSIS OF STUDY CASE

Since an application cycle goes over different operation points, an average cycle efficiency (as a function of the instant smart efficiency, defined in section I) needs to be calculated. A Matlab-Simulink model has been implemented for this purpose, see Fig. 22. The inputs of this model are: the efficiency maps of KESS and SCs described in section 5, the power generation time profile, the parameters of each device (capacity, inertia, maximum and minimum voltage, maximum and minimum speed, maximum current, etc.) and the initial SoC of both systems. The model takes the evolution of the instant SoC (voltage/speed) into account to calculate the instant efficiency and the instant stored energy.

B. STUDY CASE: WEC FARM OPERATION CYCLE

The power generated from some WECs, such as heave point absorbers, is very oscillating due to the own characteristics of the wave energy resource and the WEC itself. ESSs is one of the alternatives to improve the power supplied into the grid by compensating power fluctuations. In this study, a typical power profile of a WEC farm is considered and displayed in Fig. 23 [71]. It is important to highlight that the peaks of power generated reach around 10 times the average power value.
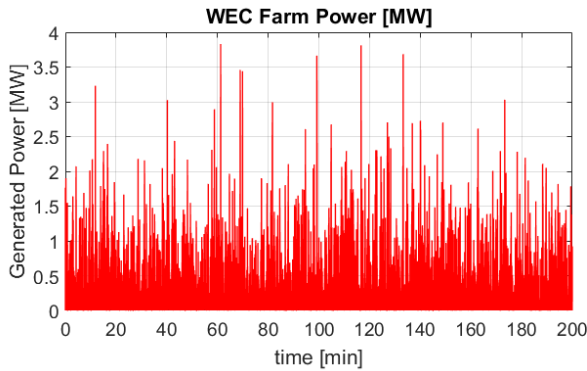

FIGURE 24. Smoothed power injected into the grid.

FIGURE 23. Instantaneous generated power profile of a WEC.

FIGURE 25. Stored power at energy storage device. Peaks define the power of energy storage device. Integrating, energy values are got.

A certain average power, calculated by means of a moving average window and presented in Fig. 24 [72], is injected into the grid, while an ESS is responsible for compensating the rest of oscillations. Although some power peaks remain in the power injected to the grid, the stability of the power system in now guaranteed. Power and energy values will define the ESS and will be obtained from the evaluation of the typical time series of wave power generation profiles. Once these parameters are defined, the storage power profile can be determined, as presented in Fig. 25. The negative power is supplied to the grid and the positive one is stored in the device [73], [74].

From the stored power profile, presented in Fig. 25, the next step is to determine power, energy levels and number of ESS modules. The methodology consists in calculating first the energy required along the complete cycle. Integrating the positive and negative cycles independently, from the profile of Fig. 25, it is obtained 7.35 kWh as the most demanding value of energy. Selecting a storage module of 125 kW of power, 0.5 kWh of energy as example, that implies a number of 15 ESS devices to be considered needed to smooth the power supplied to the grid, as obtained from (37).

$$n_{ESS} = \frac{E_{cycle}}{E_{ESS}} = \frac{7.35 \ kWh}{0.5 \ kWh} \sim 15 \qquad (37)$$

where

n_{ESS} : number of ESS modules
E_{cycle} : energy of the generation cycle
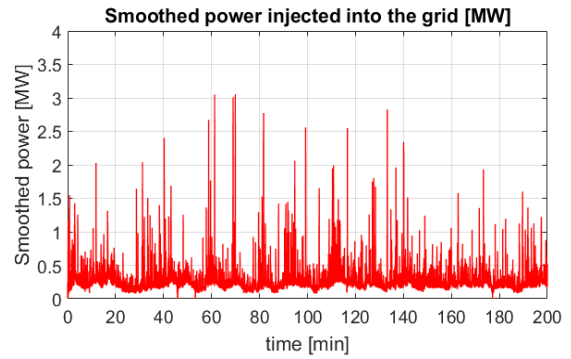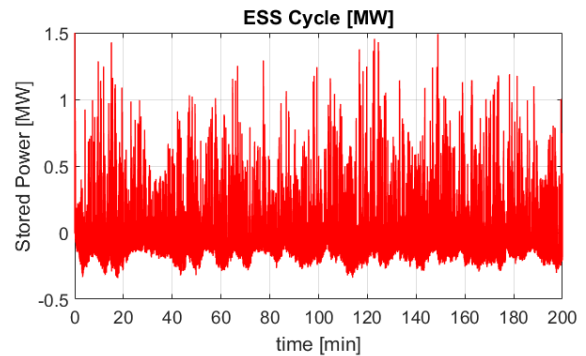E_{ESS} : usable energy of the ESS module

With this number of devices, the maximum power provided is 1.875 MW. Comparing this value with the power peaks presented in Fig. 25, it results that the 97 % of the power peaks required to the ESS could be absorbed by the set of storage devices. That level is perfectly acceptable, taking into account that usually it is not covered the 100% of the power generated because the dimensioning would lead to a huge energy storage system, not reliable for the application. Therefore, the number of devices to satisfy both conditions (energy and power) is 15. Once the ESS dimensions are determined, using the model described in sub-section 6.1 the average efficiency of both ESS technologies is calculated.

The results from this model are the evaluation of the SCs and KESS instant efficiency respect to the time (named as cycle efficiency) and the Round Trip Efficiency (RTE) [6], [9], [10], usually found in ESS datasheets.

Two different operation strategies are considered for the ESSs:

- 'All-in, all-out' strategy: All the energy storage modules supply the same power, i.e. the power supplied by each module is the instantaneous total power required by the application divided by the number of devices.
- 'Stepped Switching' strategy: This method establishes a minimum power, below which the ESS system is switched off. This minimum is related to the SoC and the instant efficiency of the device. This type of strategy improves the total efficiency of the ESS system.

The results of RTE for both ESS technologies and for both operation strategies are listed in Table 4.

TABLE 4. RTE efficiency in the operation cycle.

Technology	Control strategy	Round Trip Efficiency [%]
SCs	All-in, all-out	90.1%
KESS	All-in, all-out	65.2%
SCs	Stepped Switching	91.0%
KESS	Stepped Switching	88.7 %

VII. CONCLUSIONS

In this paper, the authors have presented a methodology to accurately compare fast energy storage technologies in terms of energy efficiency. Specifically, supercapacitors and kinetic energy storage (flywheels) have been compared by means of power losses models. These models have allowed obtaining smart global efficiency maps for each technology, which in turn can be used to assess the energy efficiency of each alternative for one or more operating cycles.

As shown in the paper, average efficiency strongly depends on the cycle and on the (over)sizing of the energy storage system. Therefore, different results have been obtained for each particular case. Generally speaking, supercapacitors have shown better efficiency than kinetic energy storage, especially when the systems have to work in a wide range of operating points. This have been especially noticeable for low power operating points, in which the performance of flywheel-based energy storage systems degrades significantly in terms of efficiency. However, another relevant difference between both technologies must be taken into account: while supercapacitors lose capacity as the charge/discharge cycles become faster (higher frequency), kinetic energy storage systems provide constant capacity over the whole frequency range. In other words, the higher the charge/discharge frequency, the more supercapacitors that are needed to match energy requirements. To perform a fair comparison between both technologies, the two systems must have the same useful energy at the expected working cycle frequency. Otherwise, the kinetic energy storage system would be oversized and thus its global efficiency would be penalized.

Finally, the analysis of a study case based on a wave energy power farm has provided realistic data of roundtrip efficiency for both technologies, confirming the previously assessed conclusions. Besides, the use of different operation strategies has provided a very different performance of the ESS, especially in KESS where the use of a 'stepping switching' strategy provides a much better efficiency than a 'all-in, all-out' strategy.

REFERENCES

[1] "Electrical energy storage," Int. Electrotech. Commun., Geneva, Switzerland, White Paper, 2011, pp. 1–78, doi: 10.1002/bse.3280020501.

[2] P. J. Grbovic, *Ultra-Capacitors in Power Conversion Systems: Applications, Analysis, and Design From Theory to Practice*. Hoboken, NJ, USA: Wiley, 2014.

[3] M. Beaudin, H. Zareipour, A. Schellenberg, and W. Rosehart, "Energy storage for mitigating the variability of renewable electricity sources: An updated review," *Energy Sustain. Develop.*, vol. 14, no. 4, pp. 302–314, Dec. 2014.

[4] E. Morofsky and P. Hamlyn, "State of the art of energy storage regulations and technology," Zaragoza, Spain, 2005.

[5] C. Krupke, J. Wang, J. Clarke, and X. Luo, "Modeling and experimental study of a wind turbine system in hybrid connection with compressed air energy storage," *IEEE Trans. Energy Convers.*, vol. 32, no. 1, pp. 137–145, Mar. 2017.

[6] *European energy Storage Technology Development Roadmap—2017*, EASE and EERA, Belgium, Brussels, 2017.

[7] V. C. Patil, P. I. Ro, and R. K. Ranganath, "End-to-end efficiency of liquid piston based ocean compressed air energy storage," in *Proc. MTS/IEEE Monterey Oceans*, Sep. 2016, pp. 1–5.

[8] C. Zhao, H. Yin, and C. Ma, "Quantitative efficiency and temperature analysis of battery-ultracapacitor hybrid energy storage systems," *IEEE Trans. Sustain. Energy*, vol. 7, no. 4, pp. 1791–1802, Oct. 2016.

[9] F. M. Gatta, A. Geri, S. Lauria, M. Maccioni, and F. Palone, "Battery energy storage efficiency calculation including auxiliary losses: Technology comparison and operating strategies," in *Proc. IEEE Eindhoven PowerTech*, Jun./Jul. 2015, pp. 1–6.

[10] T. Funaki, "Evaluating energy storage efficiency by modeling the voltage and temperature dependency in EDLC electrical characteristics," *IEEE Trans. Power Electron.*, vol. 25, no. 5, pp. 1231–1239, May 2010.

[11] G. Hong, T. Wei, and X. Ding, "Multi-objective optimal design of permanent magnet synchronous motor for high efficiency and high dynamic performance," *IEEE Access*, vol. 6, pp. 23568–23581, 2018.

[12] T. Imakawa, K. Chimata, N. Hoshi, A. Chiba, M. Takemoto, and S. Ogasawara, "Characteristic measurements of switched reluctance motor on prototype electric vehicle," in *Proc. IEEE Int. Electr. Vehicle Conf. (IEVC)*, Mar. 2012, pp. 1–8.

[13] J. Choi, I.-S. Choi, G.-H. An, and D.-J. Won, "Advanced power sharing method to improve the energy efficiency of multiple battery energy storages system," *IEEE Trans. Smart Grid*, vol. 9, no. 2, pp. 1292–1300, Mar. 2018.

[14] Q. Guo, C. Zhang, L. Li, M. Wang, L. Pei, and T. Wang, "Maximum efficiency control of permanent magnet synchronous motor system with SiC MOSFETs for flywheel energy storage," in *Proc. 19th Int. Conf. Elect. Mach. Syst. (ICEMS)*, Nov. 2016, pp. 1–5.

[15] F. Deiana, A. Serpi, I. Marongiu, G. Gatto, and J. Abrahamsson, "Efficiency assessment of permanent magnet synchronous machines for high-speed flywheel energy storage systems," in *Proc. 42nd Annu. Conf. IEEE Ind. Electron. Soc.*, Oct. 2016, pp. 4269–4274.

[16] G. Genta, *Kinetic Energy Storage: Theory and Practice of Advanced Flywheel Systems*. London, U.K.: Butterworth, 1985.

[17] Maxwell Technologies. (2012). *Maxwell Technologies Ultracapacitors, Supercapacitors, Microelectronics and High Voltage, Regenerative Power Solutions*. Accessed: Oct. 21, 2017. [Online]. Available: http://www.maxwell.com/pdf/uc/datasheets/20090227_datasheet_bc_series_1009643.5.pdf

[18] *Ioxus*. Accessed: Oct. 21, 2017. [Online]. Available: http://www.ioxus.com/english/

[19] *Ultracapacitors and Supercapacitors for Energy Storage*. Accessed: Oct. 21, 2017. [Online]. Available: https://www.skeletontech.com/

[20] N. Mohan, T. M. Undeland, and R. P. Robbins, *Power Electronics: Converters, Applications, and Design*. Hoboken, NJ, USA: Wiley, 1995.

[21] P. Moreno-Torres, M. Lafoz, M. Blanco, G. Navarro, J. Torres, and L. García-Tabarés, "Switched reluctance drives with degraded mode for electric vehicles," in *Modeling and Simulation for Electric Vehicle Applications*. Rijeka, Croatia: InTech, 2016.

[22] F. Rafik, H. Gualous, R. Gallay, A. Crausaz, and A. Berthon, "Frequency, thermal and voltage supercapacitor characterization and modeling," *J. Power Sour.*, vol. 165, no. 2, pp. 928–934, Mar. 2007.

[23] T. Tevi and A. Takshi, "Modeling and simulation study of the self-discharge in supercapacitors in presence of a blocking layer," *J. Power Sour.*, vol. 273, pp. 857–862, Jan. 2015.

[24] L. Zubieta and R. Bonert, "Characterization of double-layer capacitors for power electronics applications," *IEEE Trans. Ind. Appl.*, vol. 36, no. 1, pp. 199–205, Jan./Feb. 2000.

[25] The Mathworks Inc. (2016). *MATLAB–MathWorks*. Accessed: Oct. 21, 2017. [Online]. Available: http://www.mathworks.com/products/matlab/

[26] X. Zuo and G.-Z. Li, "Isolated voltage balancing in super-capacitor energy storage system," in *Proc. 26th Chin. Control Decis. Conf. (CCDC)*, May/Jun. 2014, pp. 5124–5128.

[27] N. Inanc, A. Derdiyok, and V. Ozbulur, "Torque ripple minimization of a switched reluctance motor including mutual inductances via sliding mode control technique," in *Proc. IEEE Int. Symp. Ind. Electron. (ISIE)*, Jul. 1997, pp. 1024–1028.

[28] L. Li, Z. Huang, W. Liu, H. Li, H. Li, and Y. Yang, "A controllable voltage equalizer with state of charge prediction for supercapacitors in large current applications," *IFAC Proc. Vol.*, vol. 19, no. 3, pp. 3623–3628, 2014.

[29] M. A. Sakka, H. Gualous, J. Van Mierlo, and H. Culcu, "Thermal modeling and heat management of supercapacitor modules for vehicle applications," *J. Power Sour.*, vol. 194, no. 2, pp. 581–587, 2009.

[30] H. Gualous, H. Louahlia, and R. Gallay, "Supercapacitor characterization and thermal modelling with reversible and irreversible heat effect," *IEEE Trans. Power Electron.*, vol. 26, no. 11, pp. 3402–3409, Nov. 2011.

[31] H. Gualous, H. Louahlia-Gualous, R. Gallay, and A. Miraoui, "Supercapacitor thermal modeling and characterization in transient state for industrial applications," *IEEE Trans. Ind. Appl.*, vol. 45, no. 3, pp. 1035–1044, May 2009.

[32] J. Lee *et al.*, "Modeling of the electrical and thermal behaviors of an ultracapacitor," *Energies*, vol. 7, no. 12, pp. 8264–8278, Dec. 2014.

[33] ANSYS. (2017). *ANSYS Fluent Software: CFD Simulation*. Accessed: Oct. 23, 2017. [Online]. Available: http://www.ansys.com/Products/Fluids/ANSYS-Fluent

[34] S. Castano, L. Gauchia, and J. Sanz-Feito, "Effect of packaging on super-capacitors strings modeling: Proposal of functional unit defined around balancing circuit," *IEEE Trans. Compon., Packag., Manuf. Technol.*, vol. 3, no. 8, pp. 1390–1398, Aug. 2013.

[35] S. M. Sharkh, M. A. Abu-Sara, G. I. Orfanoudakis, and B. Hussain, *Power Electronic Converters for Microgrids*. Singapore: Wiley, 2014.

[36] S. Zhang and X. Yu, "A unified analytical modeling of the interleaved pulse width modulation (PWM) DC–DC converter and its applications," *IEEE Trans. Power Electron.*, vol. 28, no. 11, pp. 5147–5158, Nov. 2013.

[37] E. Arango, C. A. Ramos-Paja, J. Calvente, R. Giral, and S. Serna, "Asymmetrical interleaved DC/DC switching converters for photovoltaic and fuel cell applications—Part 1: Circuit generation, analysis and design," *Energies*, vol. 5, no. 11, pp. 4590–4623, 2012.

[38] A. Wintrich, U. Nicolai, W. Tursky, and T. Reimann, *Application Manual Power Semiconductors*, 2nd ed. Ilmenau, Germany: ISLE Verlag, 2015.

[39] *For Info on Interface Power Converter IGBT*. Accessed: Nov. 3, 2017. [Online]. Available: http://shop.semikron.com/out/media/ds/SEMIKRON_DataSheet_SKM400GB17E4_22895010.pdf

[40] J. Abrahamsson, J. G. de Oliveira, J. de Santiago, J. Lundin, and H. Bernhoff, "On the efficiency of a two-power-level flywheel-based all-electric driveline," *Energies*, vol. 5, no. 8, pp. 2794–2817, Aug. 2012.

[41] V. Raulin, A. Radun, and I. Husain, "Modeling of losses in switched reluctance machines," *IEEE Trans. Ind. Appl.*, vol. 40, no. 6, pp. 1560–1569, Nov. 2004.

[42] P. Rafajdus, V. Hrabovcova, and P. Hudak, "Investigation of losses and efficiency in switched reluctance motor," in *Proc. 12th Int. Power Electron. Motion Control Conf. (EPE-PEMC)*, Aug./Sep. 2007, pp. 296–301.

[43] *SKF Group—Bearings and Units Lubrication Solutions Mechatronics Seals Services Condition Monitoring Linear Motion—SKF.Com*. Accessed: Oct. 21, 2017. [Online]. Available: http://www.skf.com/portal/skf/home

[44] T. R. Kunor and S. Taraphder, "Direct and indirect correlations in low density supercritical Lennard-Jones fluids," *Phys. A, Statist. Mech. Appl.*, vol. 383, no. 2, pp. 401–415, Sep. 2007.

[45] S. D. Calverley, G. W. Jewell, and R. J. Saunders, "Aerodynamic losses in switched reluctance machines," *IEE Proc.–Electr. Power Appl.*, vol. 147, no. 6, pp. 443–448, Nov. 2000.

[46] P. Romanazzi and D. A. Howey, "Air-gap convection in a switched reluctance machine," in *Proc. 10th Int. Conf. Ecol. Vehicles Renew. Energies (EVER)*, Mar./Apr. 2015, pp. 1–7.

[47] Y. A. Cengel and J. M. Cimbala, *Fluid Mechanics: Fundamentals and Applications*. New York, NY, USA: McGraw-Hill, 2010.

[48] E. C. Del Arco, E. Serre, P. Bontoux, and B. E. Launder, "Stability, transition and turbulence in rotating cavities," *Adv. Fluid Mech.*, vol. 41, pp. 141–195, Jan. 2005.

[49] A. Cros, E. Floriani, P. Le Gal, and R. Lima, "Transition to turbulence of the Batchelor flow in a rotor/stator device," *J. Mech.*, vol. 24, no. 4, pp. 409–424, Jul./Aug. 2005.

[50] S. Poncet, M.-P. Chauve, and R. Schiestel, "Batchelor versus Stewartson flow structures in a rotor-stator cavity with throughflow," *Phys. Fluids*, vol. 17, no. 7, pp. 075110-1–075110-15, Jul. 2005.

[51] *Vacuum Pump/Integrated OEM Vacuum Pumps for Labs*. Accessed: Oct. 23, 2017. [Online]. Available: https://www.vacuubrand.com/us/page509.html

[52] J. Pyrhönen, T. Jokinen, and V. Hrabovcová, *Design of Rotating Electrical Machines*. Hoboken, NJ, USA: Wiley, 2013.

[53] T. J. E. Miller, *Switched Reluctance Motors and Their Control*. Hillsboro, OH, USA: Magna Physics Pub., 1993.

[54] C. Carstensen, *Eddy Currents in Windings of Switched Reluctance Machines*. Aachen, Germany: Aachen Univ., 2007.

[55] A. Krings and J. Soulard, "Overview and comparison of iron loss models for electrical machines," *J. Elect. Eng.*, vol. 10, no. 3, pp. 162–169, 2010.

[56] Z. Tian, C. Zhang, and S. Zhang, "Analytical calculation of magnetic field distribution and stator iron losses for surface-mounted permanent magnet synchronous machines," *Energies*, vol. 10, no. 3, p. 320, Mar. 2017.

[57] D. Lin, P. Zhou, W. N. Fu, Z. Badics, and Z. J. Cendes, "A dynamic core loss model for soft ferromagnetic and power ferrite materials in transient finite element analysis," *IEEE Trans. Magn.*, vol. 40, no. 2, pp. 1318–1321, Mar. 2004.

[58] T. Chevalier, A. Kedous-Lebouc, B. Cornut, and C. Cester, "A new dynamic hysteresis model for electrical steel sheet," *Phys. B, Condens. Matter*, vol. 275, nos. 1–3, pp. 197–201, Jan. 2000.

[59] Q. Yu, B. Bilgin, and A. Emadi, "Loss and efficiency analysis of switched reluctance machines using a new calculation method," *IEEE Trans. Ind. Electron.*, vol. 62, no. 5, pp. 3072–3080, May 2015.

[60] M. D. Bui and U. Schaefer, "Core losses measurement technique for high frequency and flux density of switched reluctance machines," in *Proc. 20th Int. Conf. Elect. Mach.*, vol. 2012, pp. 1619–1624.

[61] L. Chen, H. Chen, and W. Yan, "A fast iron loss calculation model for switched reluctance motors," *IET Electr. Power Appl.*, vol. 11, no. 3, pp. 478–486, Mar. 2017.

[62] *Powercore For High Frequencies and e-Mobility—Thyssenkrupp*. Accessed: Oct. 23, 2017. [Online]. Available: https://www.thyssenkrupp-steel.com/en/products/electrical-steel/electrical-steel-non-grain-oriented/powercore-for-high-frequencies-and-e-mobility/powercore-a-3.html

[63] *Thin Non-Oriented Fully-Processed Electrical Steels | Non-Oriented Electrical Steel | Products | Cogent Power*. Accessed: Oct. 23, 2017. [Online]. Available: https://cogent-power.com/products/non-oriented-electrical-steel/thin-non-oriented-fully-processed-electrical-steels

[64] F. J. Perez-Cebolla, A. Martinez-Iturbe, B. Martin-del-Brio, E. Laloya, S. Mendez, and C. E. Montaño, "3D FEM characterization of a switched reluctance motor from direct experimental determination of the material magnetization curve," in *Proc. IEEE Int. Conf. Ind. Technol.*, Mar. 2012, pp. 971–976.

[65] H. Toda, K. Senda, S. Morimoto, and T. Hiratani, "Influence of various non-oriented electrical steels on motor efficiency and iron loss in switched reluctance motor," *IEEE Trans. Magn.*, vol. 49, no. 7, pp. 3850–3853, Jul. 2013.

[66] ANSYS. (2017). *ANSYS Maxwell: Low Frequency Electromagnetic Fields*. Accessed: Oct. 23, 2017. [Online]. Available: http://www.ansys.com/products/electronics/ANSYS-Maxwell

[67] R. Krishnan, *Switched Reluctance Motor Drives: Modeling, Simulation, Analysis, Design, and Applications*. Boca Raton, FL, USA: CRC Press, 2001.

[68] (2014). *For Info on Machine-Side Power Converter IGBT*. Accessed: Nov. 3, 2017. [Online]. Available: http://shop.semikron.com/out/media/ds/SEMIKRON_DataSheet_SKiiP_1203_GB172_2DFL_V3_20451115.pdf

[69] M. Göteman, J. Engström, M. Eriksson, and J. Isberg, "Optimizing wave energy parks with over 1000 interacting point-absorbers using an approximate analytical method," *Int. J. Mar. Energy*, vol. 10, pp. 113–126, Jun. 2015.

[70] M. Lafoz, M. Blanco, L. Beloqui, G. Navarro, and P. Moreno-Torres, "Dimensioning methodology for energy storage devices and wave energy converters supplying isolated loads," *IET Renew. Power Generat.*, vol. 10, no. 10, pp. 1468–1476, Nov. 2016.

[71] M. Blanco, G. Navarro, M. Lafoz, and J. I. Pérez, "How harmful is the wave energy penetration in an electric grid?" in *Proc. 12th Eur. Wave Tidal Energy Conf.*, 2017, p. 942.

[72] M. Lafoz, M. Pasquotto, P. Moreno-Torres, and M. Blanco, "Reduction of power oscillations combining energy storage with prediction techniques," in *Proc. 12th Eur. Wave Tidal Energy Conf.*, 2017, p. 823.

[73] P. Moreno-Torres, M. Lafoz, G. Navarro, M. Blanco, and L. García-Tabarés, "Sistema para el acondicionamiento de la potencia eléctrica generada en un sistema de generación undimotriz," Centro Investigaciones Energeticas Medioambientales Tecnologicas, Madrid, Spain, Tech. Rep. ES2547029 (B1), 2016.

[74] M. Lafoz, M. Blanco, and D. Ramírez, "Grid connection for wave power farms," in *Proc. 14th Eur. Conf. Power Electron. Appl. (EPE)*, Aug./Sep. 2011, pp. 1–10.

GUSTAVO NAVARRO received the degree in electronic engineering from the Universidad Politécnica de Madrid, Spain, in 2008. Since 2008, he has been a Research Engineer with CIEMAT, Spanish National Research Centre on Energy, Environment and Technology. His topics of interest are electrical drives and energy storage systems. His areas of expertise are hardware design and power electronics.

JORGE TORRES received the degree and the master's degree in mechanical engineering from the Universidad Politécnica de Madrid, Spain, in 2013 and 2016, respectively. Since 2017, he has been a Researcher with CIEMAT, Spanish National Research Centre on Energy, Environment and Technology. His research interests cover the design of electrical machines, kinetic energy storage, electrical energy storage systems, and modeling in FEM and CFD programs.

MARCOS BLANCO received the Ph.D. degree in electrical engineering from the Universidad Politécnica de Madrid, Spain, in 2018. Since 2007, he has been a Researcher with CIEMAT, Spanish National Research Centre on Energy, Environment and Technology. His research interests include power electronic converters, DSP-based control, wave energy generation, and electrical drives control.

PABLO MORENO-TORRES received the Ph.D. degree in electrical engineering from the Universidad Politécnica de Madrid in 2016. Since 2016, he has been a Research and Development Engineer with Wynnertech S.L., a power electronics company. He has participated in research projects belonging to the fields of electric vehicles, electrical machines, energy storage, and renewable energies.

MARCOS LAFOZ received the M.S. and Ph.D. degrees in electrical engineering from the Universidad Politécnica de Madrid, Spain, in 2005. Since 2008, He has been a Scientific Researcher with CIEMAT, Spanish National Research Centre on Energy, Environment and Technology. His research interests include power electronic converters, DSP-based control, wave energy generation, energy storage, and electrical drives control.

• • •